

Dominik Haberz

# Reduction of reactions in the cluster formation of $\text{TiO}_2$

## **BACHELOR'S THESIS**

to achieve the university degree of  
Bachelor's degree programme: Physik

submitted to

**Graz University of Technology**

### **Supervisor**

Prof. Dr.rer.nat. Christiane Helling,  
Institut für Theoretische Physik - Computational Physics

### **Co-Supervisor**

MSc. Sven Kiefer,  
OEAW

Graz, September 2023

## Abstract

Observations of exoplanets have increased massively in recent decades but a vast amount of their properties are unreachable for present observation methods. This creates the desire for a fully consistent 3D climate model to better interpret measurements and get the most out of them. Clouds are one important part of such a highly computationally expensive model. Their formation is connected to so-called cloud condensation nuclei (CCN) which further start with the cluster formation process of gas-phase species. The aim of this bachelor thesis is to answer how a simplification of this process for the nucleation species  $\text{TiO}_2$  is affecting the formation of CCNs. For this purpose, a closed kinetic nucleation approach was used, making several assumptions.  $\text{TiO}_2$ , being highly reactive and relatively easy to model, was chosen to be the only nucleation species. The cluster formation was studied for a homomolecular polymer growth up to a maximum size of  $N = 10$  and for the temperature range of effective  $\text{TiO}_2$ -cluster formation  $T = 400, \dots, 1000$  K. The amount of different cluster reactions available in a network is used as an indicator for its computational costs. The cloud particle number densities  $n_{CP}$  of 70 reduced networks, including between 8 and 18 reactions, were compared to the non-restricted network using 50 reactions. Reduced networks show a shift of a few hours in time in the first simulation days and a shift in the magnitude of  $n_{CP}$ , after it converged to a constant value. In order to minimize these shifts, four of the least deviating networks were combined to create 11 new networks using 12 to 24 reactions. It was achieved to keep the shift in the long-term magnitude below  $2 \cdot 10^{-2}$  for all temperatures using a combined network of 18 reactions. The results also highlighted a negative correlation between the shifts and the number of reactions. Time shifts have moderate to strong correlation. In contrast, the long-term shifts for  $T \leq 900$  K have weak, for  $T = 1000$  K have no and for  $T = 1100$  K have moderate correlation. Thus, simplifications in the cluster formation process can be performed with low effects on the long-term values of  $n_{CP}$ . In contrast, time shifts are connected with the number of reactions and therefore the computational costs.

# Contents

<b>1</b>	<b>Introduction</b>	<b>2</b>
<b>2</b>	<b>Methods</b>	<b>4</b>
2.1	Clouds and cluster formation . . . . .	4
2.2	Kinetic nucleation theory . . . . .	6
2.3	Reduced networks and notation . . . . .	7
2.4	Comparing different networks . . . . .	9
<b>3</b>	<b>Results</b>	<b>10</b>
3.1	Temporal dependancy . . . . .	11
3.2	Network combinations . . . . .	13
<b>4</b>	<b>Discussion</b>	<b>18</b>
4.1	Limitations . . . . .	18
4.2	Temporal dependancy . . . . .	19
4.3	Temperature dependancy . . . . .	20
4.4	Network combinations . . . . .	21
<b>5</b>	<b>Conclusion</b>	<b>23</b>

# Chapter 1

## Introduction

In the last 30 years, more than 5000 exoplanets were discovered (Christiansen, 2022). Some of the observations lead to a discussion about clouds and hazes on exoplanets in order to explain the measurements (Spyratos et al., 2021; Espinoza et al., 2018). Clouds have a larger opacity than the exoplanetary atmosphere, so they would scatter and absorb more radiation. Therefore the presence of clouds would have a major impact on the results and interpretation of spectroscopy measurements, which are important for studying the atmospheric gas of extrasolar planets (Helling, 2019). Aside from the influence in the observations, clouds can provide much more information. For example, current research is done on how the formation and evolution of exoplanets can be inferred from the element abundancies in clouds (Madhusudhan, 2019). Thus, clouds have a crucial influence on many parameters and the embedding of clouds in exoplanetary atmosphere models brings lots of advantages. On the other hand, a full 3D-model of an exoplanetary atmosphere, including clouds, is consuming a high amount of computational resources (Marley et al., 2013).

In this thesis, the focus was put on a possibility to reduce the computational intensity by a simplification of the cloud formation model. Cloud particles are the condensation of gas onto so-called cloud condensation nuclei (CCN) (Hudson, 1993) which form as follows. Under the right conditions, particles in the atmospheric gas can collide and build clusters which again can grow further. When they reach a certain size, the faster nucleation process sets in and they grow further until they are large enough, allowing condensation by gas-surface reactions (Helling, 2019). This work, to be more precise, investigated the cluster formation of a particular nucleation species:  $\text{TiO}_2$ . Despite  $\text{TiO}_2$  is far less abundant in exoplanetary atmospheres, it is highly reactive and directly available in the gas (Helling, 2019; Lee et al., 2015). It was also chosen to be a nucleation candidate in the works of Boulanger et al. (2019) and Sindel et al. (2022).

To accomplish this goal, this thesis dealt with the following three tasks:

1. Creation of reduced cluster formation networks for  $\text{TiO}_2$ .
2. Evaluation of the change in cloud particle number densities for the reduced networks.
3. Optimization of the networks for a minimum change in the cloud particle number density and for a maximum reduction of the cluster formation process

These tasks were fulfilled by establishing a closed kinetic nucleation network, similar to Boulanger et al. (2019) and Köhn et al. (2021). Therefore initial conditions have to be made for the atmospheric. The temperature range investigated was oriented on the efficiency of the cluster formation of  $\text{TiO}_2$ , which limits this thesis to lower temperatures Boulanger et al. (2019). The number densities of the nucleation and condensation species correspond to their solar abundancies. The main idea for the reduction of the cluster formation process is the following. The simulation setup allows polymer-polymer cluster formation, which means that clusters of size  $n$  and  $m$  can be combined into a cluster of size  $l = n + m$  (Boulanger et al., 2019). This allows a huge amount of combinations, how a cluster can grow from its monomer to a higher cluster size. The motivation for this thesis is the assumption, that not all paths of growing are equally likely, leading to more relevant and less relevant reactions. An elimination of the less relevant reactions is connected to less computational effort but it might also change the resulting cloud particle number density. Thus, this work investigated how the simplification affects the cloud particle number density by comparing many different reduced network simulations to a simulation including all reactions. To keep the number of different cluster growing possibilities within the scope of this thesis, the maximum cluster size was set to  $N = 10$ . The physical meaning of this number is that clusters of sizes  $N \geq 10$  were assumed to be far less likely to fall apart and are therefore quickly growing further to CCN's. This number could be extended to  $N = 15$ , as the backward rates can be at least calculated for clusters up to this size (Sindel et al., 2022). For the chosen  $N = 10$  in this thesis the number of different cluster formation possibilities is 70 (see section 2.3). The aim was to find the best of these networks and combine them to even better.

# Chapter 2

## Methods

This chapter starts with an explanation about cloud formation and is then giving a more detailed insight into the cluster formation process. Afterwards, the kinetic nucleation network is introduced which builds the basis of the simulations done in this thesis. Also the approach of this thesis to modify and reduce the cluster formation network for  $\text{TiO}_2$  is explained and a notation for naming these networks is introduced. In the end, two parameters were elaborated to measure the change in the cloud particle number density obtained from two different network simulations.

### 2.1 Clouds and cluster formation

As already mentioned in chapter 1, there is no clear evidence for exoplanetary clouds but they would have a huge impact on the whole system of an exoplanet. Clouds are chemically very rich, resulting in an optically very thick layer which further leads to a change in the temperature profile and an increase in absorption and scattering (Marley et al., 2013). In addition, the source material species of cloud particles are getting less abundant in atmospheric layers where clouds are formed Helling (2019).

Among others, the cloud formation has a minimum requirement, the occurrence of cloud condensation nuclei (CCN). These act as seeds for the formation of cloud particles (Hudson, 1993). Condensation species like metal oxides, silicates, carbon species, high temperature condensates and sulfur species condensate onto CCNs through gas-surface reactions and grow to  $\mu\text{m}$ -sized cloud particles (Helling, 2019). CCNs are in turn formed as follows and as shown in Figure 2.1.

After a collision of two particles, called nucleation species, they can stick together and form a cluster. This cluster can grow again with a monomer (Helling, 2019) or, as assumed in this thesis and the works of Boulanger et al. (2019) and Köhn et al.

(2021), with another cluster. Clusters can grow but also fall apart, which leads to a net rate in forward direction if the conditions for cluster formation are met or in backward direction otherwise (Boulangier et al., 2019). In this work it is assumed that there is a certain cluster size  $N$ , for which all clusters of size  $N$  and larger have far higher net forward rates than the cluster of size  $N - 1$ . This assumption is supported by the decrease of the Gibbs free energy for larger clusters, which leads to lower backward rates for larger clusters (Lee et al., 2015). Once a cluster greater or equal to  $N$  is formed, it will efficiently nucleate to even larger sizes until it is big enough for condensation – A cloud condensation nuclei has formed (Helling, 2019).

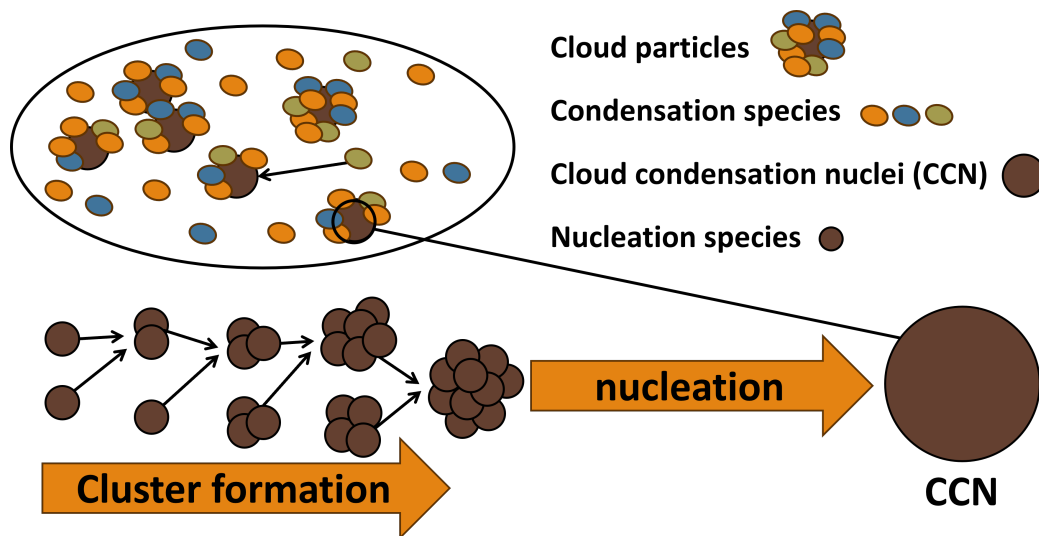


Figure 2.1: Schematic description of the cloud formation process. Monomers and small polymers are growing to a cluster of size  $N$  by cluster formation. Due to nucleation this cluster gets larger until it reaches the size of a cloud condensation nuclei (CCN). The surrounding condensation species are then condensing onto the CCN until a cloud particle is formed (Helling, 2019)

In particular, this thesis only allows homomolecular cluster formation and nucleation of  $\text{TiO}_2$  as it is done in Sindel et al. (2022). The maximum cluster size which can be formed during cluster formation is restricted to  $N = 10$  in order to keep the number of possible reactions forming this cluster size within the scope of this thesis. This has also been assumed in Boulangier et al. (2019) and Köhn et al. (2021).

## 2.2 Kinetic nucleation theory

For the calculation of the cloud particle number densities the same closed kinetic nucleation approach as in Boulangier et al. (2019) and Köhn et al. (2021) is used. The meaning of closed is that no interactions between other gas-phase species and no mass exchange takes place to or from the outside of the network (Boulangier et al., 2019). The theory for 1D systems from Tsai et al. (2017), using a zero spatial transport flux, results in the ordinary differential equation Equation 2.1a. This equation describes the change in the number density of a cluster of size  $i$  for one timestep. The production rate  $P_i$  and the loss rate  $L_i$  are further split up using the forward rate  $R_i^+$  and backward rate  $R_i^-$  for each cluster of size  $i$  (see Equation 2.1b). The additional splitting in four sums is used to show the four types of different reactions shown in Figure 2.2. The number density of a cluster of size  $i$  is increased when two smaller clusters form a cluster of size  $i$  (forward reaction) or when a larger cluster is falling apart (backward reaction) and one of the two resulting clusters has size  $i$ . On the other hand the number density decreases when it is falling apart in two smaller clusters (backward reaction) or when it is further growing together with another cluster (forward reaction).

$$\frac{dn_i}{dt} = P_i - L_i \quad (2.1a)$$

$$= \sum_{i=g+h} R_{g,h}^+ \cdot n_g \cdot n_h - \sum_{i=g+h} R_{g,h}^- \cdot n_i - \sum_{l=i+j} R_{i,j}^+ \cdot n_i \cdot n_j + \sum_{l=i+j} R_{i,j}^- \cdot n_l \quad (2.1b)$$

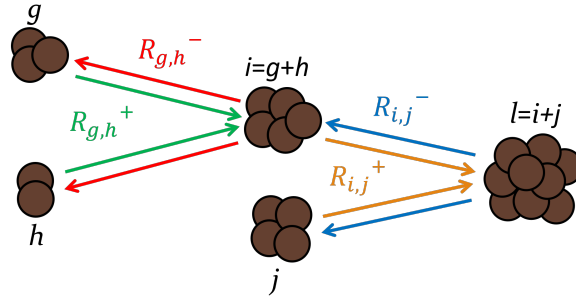


Figure 2.2: Schematic of the four different ways how the number density of a cluster of size  $i$  can be changed.  $R_{g,h}^+$  and  $R_{i,j}^+$  are the forward rates of forming clusters of size  $i = g + h$  and  $l = i + j$ , respectively.  $R_{g,h}^-$  and  $R_{i,j}^-$  are the backward rates of clusters falling apart into the sizes  $g$  and  $h$  and the sizes  $i$  and  $j$ , respectively.

The forward rate (see Equation 2.2) for two colliding clusters of size  $i$  and  $j$  is the product of the total cross section of these clusters with their average relative speed (Boulangier et al., 2019). Due to a lack of information the sticking coefficient had to be set to one. Therefore it was assumed that all collisions lead to a cluster formation. The backward rate is calculated by Equation 2.4 using the concept of minimising the Gibbs free energy. This approach is picked up by many works in this research field (Boulangier et al., 2019; Köhn et al., 2021; Lee et al., 2015; Tsai et al., 2017; Sindel et al., 2022). This method assumes that the system has enough time between the reactions to relax to the minimum energy state. In addition, no effects like a collision can trigger the destruction process (Boulangier et al., 2019).

Forward reaction rate (Boulangier et al., 2019):

$$R_{i,j}^+ = \pi (r_i + r_j)^2 \cdot \bar{v}_{i,j} \quad (2.2)$$

with  $r_i$  denoting the radius of a cluster of size  $i$  and mass  $m_i$ . The last term is the average relative speed:

$$\bar{v}_{i,j} = \sqrt{\frac{8k_B T}{\pi \mu_{i,j}}}, \text{ with reduced mass } \mu_{i,j} = \frac{m_i m_j}{m_i + m_j} \quad (2.3)$$

Backward reaction rate (Boulangier et al., 2019):

$$R_{i,j}^- = R_{i,j}^+ \cdot \frac{P^\circ}{k_B T} \exp\left(\frac{G_{i+j}^\circ - G_i^\circ - G_j^\circ}{k_B T}\right) \quad (2.4)$$

The  $^\circ$  is denoting a standard pressure of  $P^\circ = 10^5$  Pa, thus  $G_i^\circ$  means the Gibbs free energy calculated at standard pressure for a cluster of size  $i$ .  $k_B = 1.3806 \cdot 10^{-23}$  J K<sup>-1</sup> is the Boltzmann constant (Newell and Tiesinga, 2019) and  $T$  the gas temperature.

Equation 2.1a leads to a set of coupled ODE's which can be solved for initial conditions, which are introduced in chapter 3 for each simulation.

## 2.3 Reduced networks and notation

With the calculation of the forward rates  $R^+$  and backward rates  $R^-$ , the approach of this thesis for reducing reactions from a simulation network can be implemented. The schematic in Figure 2.2 shows the rates to and away from a cluster of size  $i$ . Setting one of these rates to zero is the same as removing the according reactions from the network.

In section 2.1 it was explained that a  $\text{TiO}_2$  cluster in the gas has many probabilities of growing to a higher cluster size. Thus, there is not only one path to grow for a monomer to the maximum cluster size  $N$ . Based on this, it was assumed that clusters in the full polymer network would use some reactions more often than others, despite all reactions were available for them. This motivated the assumption for this thesis that there exist dominant paths which were more important than others for the cluster formation.

For this work all non-cyclic paths have been determined using the following method. It also introduces a notation for uniquely describing paths and therefore reduced networks. An example for this notation is shown in Figure 2.3i.

One path is a list of integers  $n_i$  which represent the cluster size after  $i$  collisions.  $i$  is also the position of the integer in the list starting with 0. Therefore, the first position is the initial cluster size  $n_0 = 1$ . For the collision  $i$  there are  $i$  possibilities for the cluster of size  $n_i$  to grow. For each possibility  $j = 0, \dots, i - 1$ , the next size  $n_i$  has to be the sum of the cluster before the reaction of size  $n_{i-1}$  and a cluster of the size  $n_j$ . A path is complete when the cluster size at the last position is equal to  $N$ . Paths where the cluster size at the last position is greater than  $N$  are not considered.

Non-cyclic means that only forward paths without the occurrence of destruction were considered because an additional cycle would lead to a path which is less likely to be dominant. For example the path  $[1,2,4,6]$  is for sure more efficient than the path  $[1,2,4,2,6]$  and therefore such paths are neglected. The calculation was fully performed using  $N = 5$  as an example in Figure 2.3ii and lead to three paths. It should be highlighted that for this thesis no reactions for clusters to higher sizes than  $N$  were included, although this would be for sure an non-physical behavior.

Reduced networks are now created for all paths up to  $N = 10$  by setting all reaction rates to zero which are not in the corresponding path. This lead to 70 reduced networks which were investigated within this thesis.

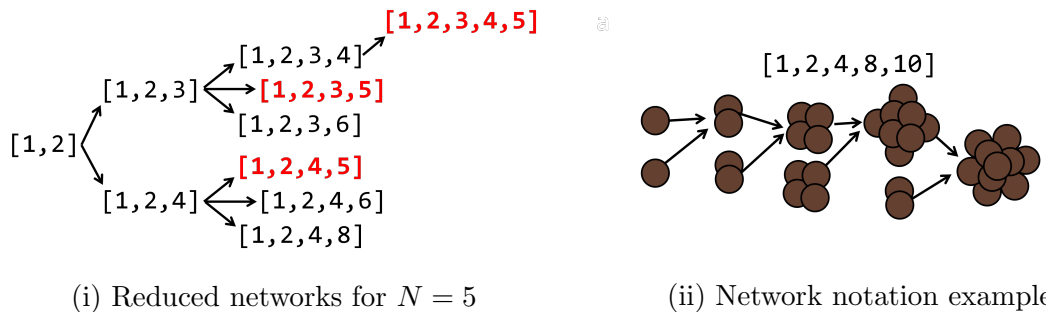


Figure 2.3: Progress of determining all paths up to  $N = 5$  with red marked resulting paths in (i) and using the path notation, for which an example is shown in (ii).

## 2.4 Comparing different networks

The simulation results in the time evolution of the cloud particle number density. To compare the results of two different networks with each other, the parameters  $p_{rise}$  and  $p_{static}$  were introduced to describe the deviation. In Figure 2.4 fictional results for the cloud particle number densities of two simulation networks show how these parameters can be interpreted. The results are therefore split in two sections: The rising section and the static section. The static section is defined by the time when the rate of the cloud particle number density is less than a certain tolerance. The rising section is then defined from the simulation start until the static section begins.

The comparison values are calculated by Equation 2.6 for  $p_{static}$  and by Equation 2.5 for  $p_{rise}$ . As showed in Figure 2.4 the value  $p_{static}$  is an indicator for a deviation in the static section and  $p_{rise}$  for the rising section.  $p_{rise}$  can also be used as an indicator for a shift in time. This is because of the fast rising at the beginning, leading to a large increase in  $p_{rise}$  even for short time shifts.

$$p_{rise} = \max_{t \leq t_{static}} \left\{ \log_{10} \left( \frac{n_{CP}^I(t)}{n_{CP}^{II}(t)} \right) \right\} \quad (2.5)$$

$$p_{static} = \log_{10} \left( \frac{\bar{n}_{CP}^I}{\bar{n}_{CP}^{II}} \right), \quad (2.6)$$

$\bar{n}_{CP}^I$  is defined as the mean value of  $n_{CP}(t)$  of the network  $I$  for  $t \geq t_{static}$

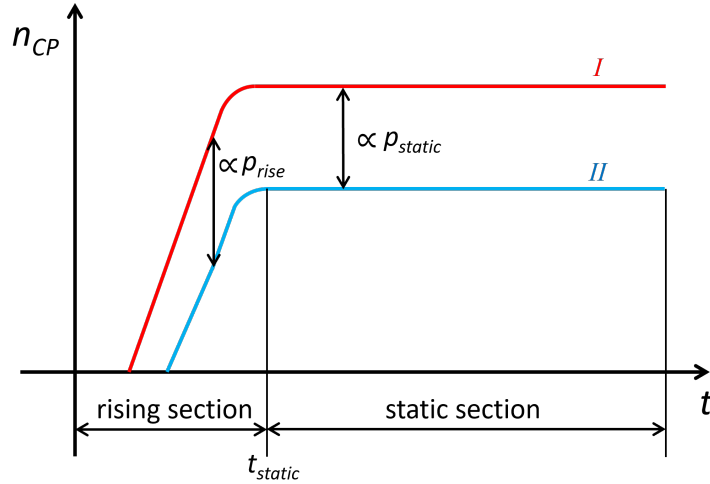


Figure 2.4: Schematic of the results for the cloud particle number densities  $n_{CP}$  of two networks  $I$  (red) and  $II$  (blue). The rising and static section are marked and defined by the time  $t_{static}$  since when  $n_{CP}$  is constant in time. It is shown which deviations the two comparison values  $p_{rise}$  and  $p_{static}$  are indicating

# Chapter 3

## Results

This chapter shows the simulation results for three different kinds of networks which differ only in the reactions available in the cluster formation process. The second and third type are both reduced networks. For these types a notation was created to better distinguish one from each other (see section 2.3).

1. A full polymer network including all forward and backward reactions which is further called original network.
2. Networks which are reduced to a single specific cluster formation path. Therefore, only reactions which are at least necessary to build the maximum cluster of size  $N$ , starting from monomers, are included into this kind of networks. For instance, the network 1-2-4-6-10 requires the monomer-monomer-, dimer-dimer- and tetramer-hexamer-reactions. Reactions are included in forward and backward direction. These kind of networks are further called path networks.
3. Networks reduced to multiple cluster formation paths. This kind of networks is therefore just an extension of the second one. Here, the union of the reactions of the individual paths are used. They are further called combined networks.

For the simulation, the set of coupled ODE's from section 2.2 were solved using 'DLSODES' developed from Hindmarsh et al. (2023).  $N = 10$  was chosen to be the maximum cluster size for cluster formation as explained in section 2.1. This thesis only considers  $\text{TiO}_2$  as a cluster formation and nucleation species. The initial number density of  $\text{TiO}_2$  in the gas was set to  $n_{\text{TiO}_2} = 10^3 \text{ cm}^{-3}$  as it is the same abundancy Köhn et al. (2021) used for their polymer kinetic nucleation model. In addition, Fe was also added with an abundancy of  $n_{\text{Fe}} = 3 \cdot 10^5 \text{ cm}^{-3}$  to the gas because Fe and FeO were used beside  $\text{TiO}_2$  as condensation species (Helling and Woitke, 2006). The fast and effective condensation properties of these species ensured an effective

condensation for the simulation. There is no claim for this work on the correctness of the condensation process, since the focus is on the cluster formation. Therefore, no more condensation species were added, although there are many other species mentioned in Helling and Woitke (2006).

Simulations were performed for the temperatures  $T = 400, 500, \dots, 1100$  K for all networks. For temperatures below, the kinetic energy of the clusters and therefore the forward rates are too low for an effective cluster formation. For even higher temperatures, an increased cluster evaporation occurs which leads to an increase in the backward rate and again an ineffective cluster formation (Boulangier et al., 2019).

To compare the reduced networks with the original network the parameters  $p_{rise}$  (see Equation 2.5) and  $p_{static}$  (see Equation 2.6) were used.

### 3.1 Temporal dependancy

The first two figures compare the time dependancy of the cloud particle number density  $n_{CP}$  of the original network and the path networks. For this purpose, the temperature  $T = 800$  K was picked because at this temperature the number density  $n_{CP}$  shows a very general behavior over time for most of the networks. The plots for all temperatures can be found in Figure 5.1.

The aim of Figure 3.1 is to show the curve progression of  $n_{CP}$  and how the 70 path networks (grey lines) differ in time from the original network (red line). In general,  $n_{CP}$  is rising quickly for all networks within the first one to two simulation days. For example, the original network reaches 67% in the first 1.5 days and 99% in the first 80 days. The networks are then slowly converging with a constant rate to a maximum value. When the maximum is reached, the rate drops to zero. The constant converging rate is too low to see a change in  $n_{CP}$  at shorter time scales of roughly  $10^6$  s to  $10^{10}$  s for most of the networks. How long it takes for a reduced network to reach the magnitude of the original network, if ever, is strongly depending on the network and on the temperature.

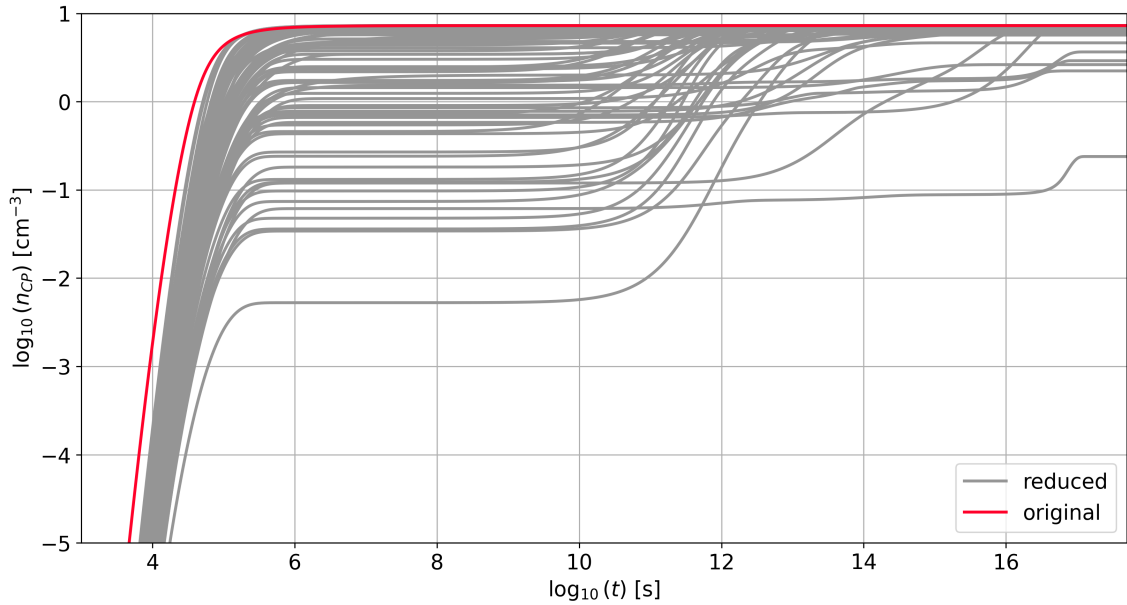


Figure 3.1: Logarithmic values of the cloud particle number densities over the logarithmic time. The original network (red line) is shown with all 70 path networks (grey lines) for values above  $10^{-5} \text{ cm}^{-3}$  and up to  $5 \cdot 10^{17} \text{ s}$ .

Figure 3.2 shows a smaller but more detailed section of the same simulations for just the original and the five best path networks in the static section. Best is hereby denoted to the lowest values of  $p_{rise}$  (see Equation 2.5). The fastest networks 1-2-4-6-10 (green), 1-2-4-8-10 (orange) and 1-2-3-5-10 (pink) are reaching the original network after about one to three days. The next network 1-2-3-5-7-10 takes about five to seven days and the network 1-2-4-6-8-10 takes about 50 to 70 days. The path network 1-2-4-6-10 (green) has the shortest temporal difference to the original network, which is 5 h at its maximum. The original network reaches  $n_{CP} = 4.2 \text{ cm}^{-3}$  after 27 h while 1-2-4-6-10 takes 31 h to reach the same value.

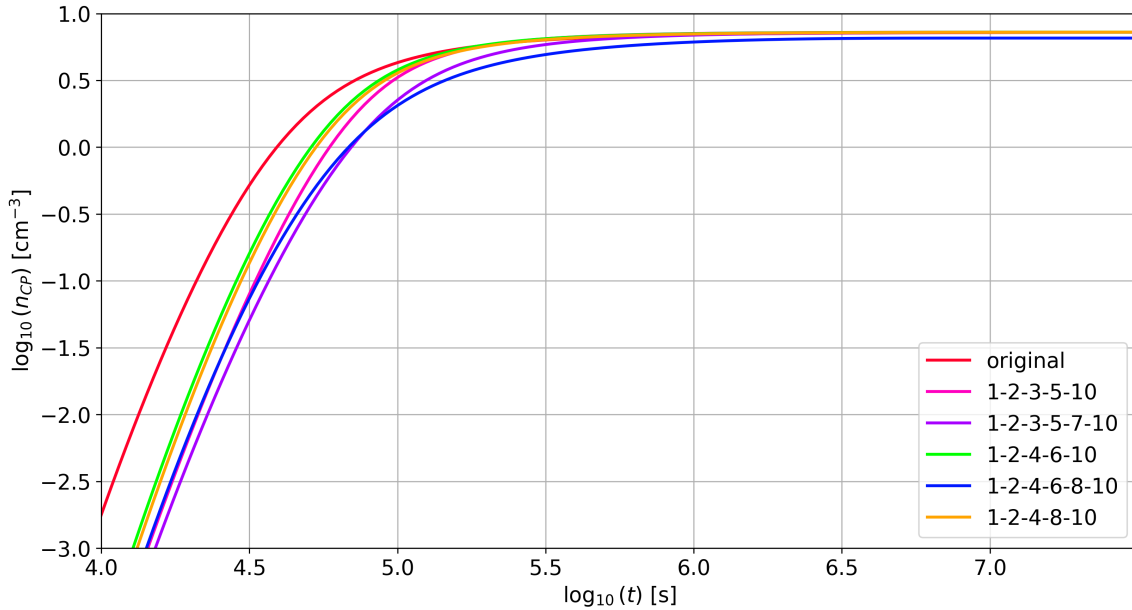


Figure 3.2: Detailed section of logarithmic values of the cloud particle number densities over the logarithmic time. The original network (red line) is shown with the five least time deviating path networks (colored lines) for values above  $10^{-3} \text{ cm}^{-3}$  over one year simulation time.

## 3.2 Network combinations

The comparison values  $p_{rise}$  (see Equation 2.5) and  $p_{static}$  (see Equation 2.6) were calculated according to section 2.4 for each path network and temperature. The results for  $p_{rise}$  stayed within the same scale for all networks and in contrast,  $p_{static}$  differs in orders of magnitude for the different networks. Thus, for  $p_{static}$  the logarithmic value is plotted and for  $p_{rise}$  not. Figure 3.3 and Figure 3.4 show on the one hand in their subfigures (i) on which scale the path networks differ from the original network for different temperatures. On the other hand, they also show below in their subfigures (ii) the results of the network optimization which was performed as follows.

In a first step, the comparison values  $p_{static}$  and  $p_{rise}$  were determined and plotted over temperature for all 70 path networks (see Figure 3.3i and Figure 3.4i). To ensure the overview but still see the general trend, only networks which lead to the smallest value for at least one temperature were colored and the others were greyed out. For  $p_{rise}$  two and for  $p_{static}$  five networks are considered to be the best. These networks build the basis for the decision about which networks should be combined. As it will

be explained in section 4.4, the following four networks were combined: 1-2-4-6-10 (a), 1-2-4-5-10 (b), 1-2-3-5-6-8-9-10 (c) and 1-2-3-4-8-9-10 (d). The letters a,b,c and d are further used for naming the combined networks. For example (abd) is the name of the network containing the union of the reactions of the path networks (a), (b) and (d). This combination lead to eleven combined networks for which  $p_{static}$  and  $p_{rise}$  were again plotted over temperature (see Figure 3.3ii and Figure 3.4ii). The four best path networks were also added to these figures (dashed lines).

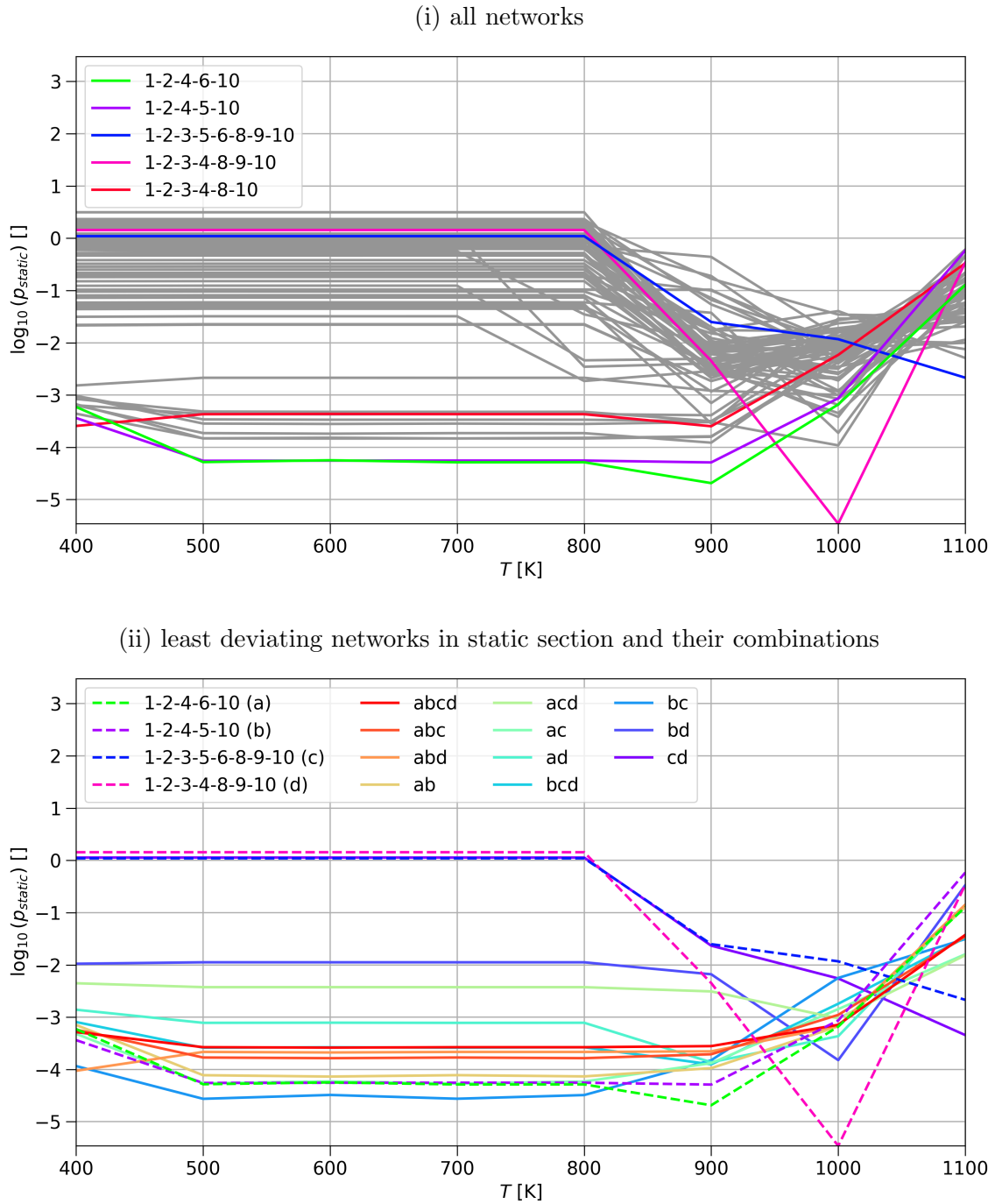
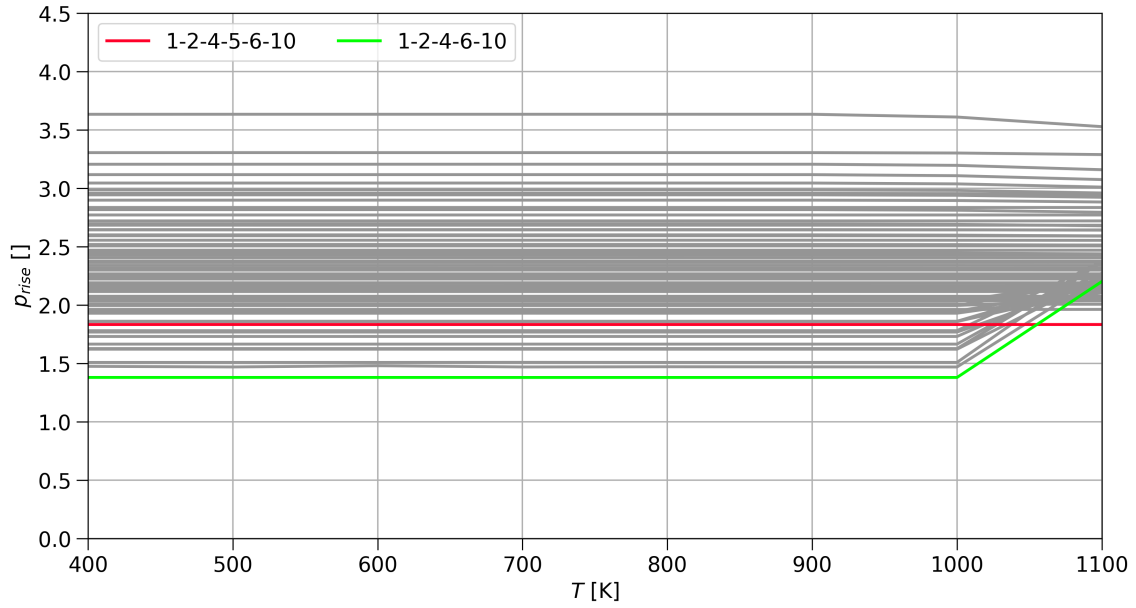
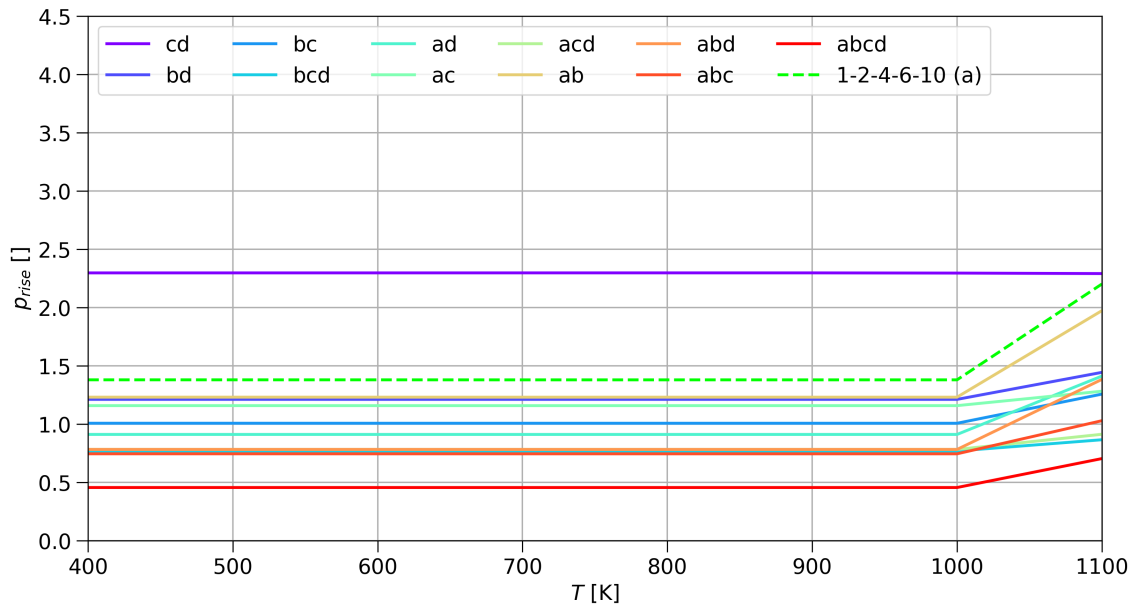


Figure 3.3: Logarithmic value of  $p_{static}$  for the temperatures  $T = 400, \dots, 1100$  K. In (i) all 70 path networks (grey lines) are shown and networks with the smallest value for at least one temperature were colored. Four of the highlighted networks in (i) are again plotted in (ii) using dashed lines together with all of their combinations using solid lines.



(i) all networks



(ii) least deviating networks in static section and their combinations

Figure 3.4: Comparison value  $p_{rise}$  for the temperatures  $T = 400, \dots, 1100$  K. In (i) all 70 path networks (grey lines) are shown and networks with the smallest value for at least one temperature were colored. In (ii) the combinations of four of the least deviating networks in the static section are shown using solid lines. Network 1-2-4-6-10 (a) is added as the only least deviating network in the rising as well as in the static section.

The comparison values  $p_{static}$  and  $p_{rise}$  were collected for the networks (a), (b), (c), (d) and their combinations in Table 3.1. The values for  $p_{rise}$  are constant up to 1000 K. In the range 500,  $\dots$ , 800 K the values of  $p_{static}$  are varying less than 20%. Due to the logarithmic scaling, this is small enough so that this temperature range is represented by 700 K. Therefore, just the temperatures 400, 500, 700, 1000 and 1100 K are shown for  $p_{static}$  in Table 3.1 to ensure the overview of the table.

The results suggest that there is a correlation between  $p_{rise}$  and the number of reactions, so the correlation coefficient (Kohn, 2005) was calculated for each temperature for both comparison values. The calculations were added on the bottom of the table in the last row.

Table 3.1: Comparison values  $p_{static}$  and  $p_{rise}$  and the number of reactions  $N_R$  for the networks 1-2-4-6-10 (a), 1-2-4-5-10 (b), 1-2-3-5-6-8-9-10 (c) and 1-2-3-4-8-9-10 (d) and their combinations for  $T = 400, \dots, 1100$  K. The last row, separated by double lines contains the correlation coefficient  $R$  for each temperature between the comparison values and  $N_R$ . These values are subject to uncertainties due to assumptions made in the simulation model.

name	$N_R$	$p_{static}$					$p_{rise}$	
		400 K	700 K	900 K	1000 K	1100 K	$\leq 1000$ K	1100 K
a	8	$6 \cdot 10^{-5}$	$5 \cdot 10^{-5}$	$2 \cdot 10^{-5}$	$7 \cdot 10^{-4}$	$1 \cdot 10^{-1}$	1.4	2.2
b	8	$4 \cdot 10^{-4}$	$6 \cdot 10^{-5}$	$5 \cdot 10^{-5}$	$9 \cdot 10^{-4}$	$6 \cdot 10^{-1}$	1.8	1.8
c	14	$1 \cdot 10^{+0}$	$1 \cdot 10^{+0}$	$2 \cdot 10^{-2}$	$1 \cdot 10^{-2}$	$2 \cdot 10^{-3}$	2.6	2.6
d	12	$1 \cdot 10^{+0}$	$1 \cdot 10^{+0}$	$4 \cdot 10^{-3}$	$3 \cdot 10^{-6}$	$3 \cdot 10^{-1}$	2.6	2.6
ab	12	$7 \cdot 10^{-4}$	$8 \cdot 10^{-5}$	$1 \cdot 10^{-4}$	$7 \cdot 10^{-4}$	$1 \cdot 10^{-1}$	1.2	2.0
ac	20	$5 \cdot 10^{-4}$	$5 \cdot 10^{-5}$	$1 \cdot 10^{-4}$	$1 \cdot 10^{-3}$	$2 \cdot 10^{-2}$	1.2	1.3
ad	18	$1 \cdot 10^{-3}$	$8 \cdot 10^{-4}$	$1 \cdot 10^{-4}$	$4 \cdot 10^{-4}$	$1 \cdot 10^{-1}$	0.9	1.4
bc	20	$1 \cdot 10^{-4}$	$3 \cdot 10^{-5}$	$1 \cdot 10^{-4}$	$6 \cdot 10^{-3}$	$3 \cdot 10^{-2}$	1.0	1.3
bd	18	$1 \cdot 10^{-2}$	$1 \cdot 10^{-2}$	$7 \cdot 10^{-3}$	$2 \cdot 10^{-4}$	$3 \cdot 10^{-1}$	1.2	1.4
cd	18	$1 \cdot 10^{+0}$	$1 \cdot 10^{+0}$	$2 \cdot 10^{-2}$	$6 \cdot 10^{-3}$	$5 \cdot 10^{-4}$	2.3	2.3
abc	24	$6 \cdot 10^{-4}$	$2 \cdot 10^{-4}$	$2 \cdot 10^{-4}$	$1 \cdot 10^{-3}$	$4 \cdot 10^{-2}$	0.7	1.0
abd	22	$9 \cdot 10^{-5}$	$2 \cdot 10^{-4}$	$2 \cdot 10^{-4}$	$7 \cdot 10^{-4}$	$1 \cdot 10^{-1}$	0.8	1.4
acd	24	$4 \cdot 10^{-3}$	$4 \cdot 10^{-3}$	$3 \cdot 10^{-3}$	$9 \cdot 10^{-4}$	$2 \cdot 10^{-2}$	0.8	0.9
bcd	24	$8 \cdot 10^{-4}$	$3 \cdot 10^{-4}$	$1 \cdot 10^{-4}$	$2 \cdot 10^{-3}$	$3 \cdot 10^{-2}$	0.8	0.9
abcd	28	$5 \cdot 10^{-4}$	$3 \cdot 10^{-4}$	$3 \cdot 10^{-4}$	$7 \cdot 10^{-4}$	$4 \cdot 10^{-2}$	0.5	0.7
$R$		-0.30	-0.30	-0.15	-0.07	-0.59	-0.66	-0.78

# Chapter 4

## Discussion

The results of chapter 3 are discussed in the following sections starting with the limitations of this work. Then the temporal behavior of  $n_{CP}$  is analysed and the similarities between networks with a high value of  $p_{static}$  are pointed out. Afterwards, the temperature dependency of  $n_{CP}$  is explained for path networks.

### 4.1 Limitations

In order to stay within the scope of this thesis, some restrictions had to be made. In this chapter, the most important limitations were discussed.

The most important restriction of this bachelor thesis is that only Fe and FeO have been implemented, beside  $TiO_2$ , as condensation species. This is because of the consumption of Ti and O by condensation species like FeO or others containing titanium and oxygen, e.g. SiO, MgO or  $CaTiO_3$  (Helling, 2019). Therefore the abundancies of Ti and O are higher in this bachelor thesis than they actually are on exoplanets. This also leads to a higher abundance of  $TiO_2$  and so to more mass available in the cluster formation process. In addition to this, smaller particles are growing faster because of a larger surface to volume ratio, which means that clusters are growing faster to the size of cloud particles than existing cloud particles are growing to larger sizes. The consequence for this bachelor thesis is that the absolute value of the determined cloud particle number densities occur to be higher than they are on real exoplanets, where many other condensation species exist.

In addition, the restriction of  $TiO_2$  to be the only cluster formation and nucleation species is a huge simplification for this work. This is because clusters of  $TiO_2$  are simply adding up during cluster formation (Köhn et al., 2021). Therefore, these processes are easier to understand and interpret. On the other hand,  $TiO_2$  is not

nucleating efficiently for temperatures above 1000 K and titanium has low abundancies (Boulangier et al., 2019; Köhn et al., 2021). Because of this  $\text{TiO}_2$  might be less relevant than other nucleation species.

Another important restriction is that the simulation network was chosen to be a closed network, thus no mass is exchanged to or from the outside of the network. Therefore, this restriction has a guaranteed impact on the time evolution of the cloud particle number density as it remains constant when the source material (smaller clusters) is fully depleted. This is a clear non-physical behavior as heavier cloud particles would start sinking due to the gravitational force and then evaporate in layers of higher temperatures. The evaporated elements would rise again and replenish the source material for cluster formation (Helling, 2019). This is also likely to impact the efficiency of the reduced networks as lower cluster sizes would have higher number densities due to the element replenishment and reactions depending on such clusters would have higher rates than calculated in this work.

Furthermore, there is the restriction to the highest cluster size of  $N = 10$  of the cluster formation network. For higher  $N$  the number of different paths to reach  $N$  explodes quickly. For example,  $N = 10$  results in 70 different paths but for  $N = 15$  there would be 1745 different possibilities. Sindel et al. (2022) calculated the Gibbs free energies, which are necessary for determining the backward rates of the clusters, up to  $N = 15$ . Therefore, it would be possible to upscale this work to a higher  $N$ .

## 4.2 Temporal dependancy

The temporal behavior of  $n_{CP}$  can be explained by looking at the initial conditions of the simulations and the restriction to a closed network (see section section 4.1). Each simulation is starting with only  $\text{TiO}_2$  monomers which are rapidly forming  $(\text{TiO}_2)_2$  and other small clusters. Since Sindel et al. (2022) and Lee et al. (2015) showed that the Gibbs free energy is decreasing with larger cluster sizes up to  $N = 10$ , the backward rates of larger clusters are lower than those of smaller clusters. Therefore, larger clusters grow on the cost of smaller clusters and thus their number densities decrease. At the beginning of the simulation, the densities are high enough and ensure an efficiently strong growth of  $n_{CP}$  for all networks in Figure 3.1. Once a cluster of size ten is formed, it is nucleating to a CCN and a cloud particle is formed from it, resulting in a continuous outflow of material from the ongoing cluster formation. Furthermore, no new monomers can be created because the network was restricted to be a closed network. At some point in simulation time, the number densities of the smaller clusters are too low to form  $(\text{TiO}_2)_{10}$ -clusters efficiently. Then the rate of the cloud particle number density drops in orders of magnitude. Within the conditions and benchmark temperature of  $T = 800$  K, the timesteps needed to see a change in

$n_{CP}$  is around hundreds of years, which is in huge contrast to the time of 1.5 days to reach 67% of the maximum  $n_{CP}$  for the original network. The time scales in this work are supported by the results of Boulangier et al. (2019), in which a converging time for the cluster formation of  $(\text{TiO}_2)_{10}$  of roughly 20 days were stated for  $T = 1000$  K. Figure 5.1vii in the appendix shows for this thesis that after 20 days 98% of the maximum  $n_{CP}$  is reached for the original network.

An analysis of the comparison value  $p_{static}$  for  $T = 800$  K shows that there is a connection between high values and some reduced networks. As  $p_{static}$  is almost constant for lower temperatures, this analysis holds also for all temperatures smaller than 800 K.  $p_{static} = 0.33$  splits the 70 path networks in two halves, which means that there are 35 networks having a value higher than it and are therefore differing more from the original network. 80% of these networks have in common that the final  $(\text{TiO}_2)_{10}$ -clusters have to be build from the clusters  $(\text{TiO}_2)_9$  and  $\text{TiO}_2$ . This seems reasonable as the number density of  $\text{TiO}_2$  is decreasing much earlier than the one of  $(\text{TiO}_2)_9$  is rising (Lee et al., 2015).

Figure 5.1 of the appendix shows that the time for  $n_{CP}$  to reach its maximum is in general the shortest for 1000 K and gets higher for lower and higher temperatures. For lower temperatures, the collision rate decreases and for higher temperatures the clusters become less stable.

Beside the shift in the magnitude of  $n_{CP}$  for a reduced and the original network there is a shift in time. The rising of  $n_{CP}$  starts earlier in the original network than in the reduced networks. One reason could be that the original network allows the building of the  $(\text{TiO}_2)_{10}$ -cluster for all smaller clusters and a reduced network like the monomer path 1-2-3-4-5-6-7-8-9-10 can only produce a cluster of size ten from a cluster of size nine which again has to be produced from the next smaller cluster before and so on. Figure 3.2 shows that networks containing a small number of reactions like 1-2-4-6-10 (green) and 1-2-4-8-10 (orange) have a smaller time shift. These networks have two advantages, they only need a minimum amount of steps to build size ten and the number densities of the building clusters are high because the cluster material is distributed on fewer different cluster sizes.

### 4.3 Temperature dependancy

The dependancy of  $n_{CP}$  on the temperature is strongly varying on the network under consideration. Therefore, the following discussion is mostly focusing on the main trend of all networks rather than on the behavior of individual networks.

For the static section, the comparison value  $p_{static}$  shows almost no changes for lower temperatures up to 900 K. It appears that 70% of the networks have values larger

than  $10^{-1}$  and only 14 % have values smaller than  $10^{-3}$ . Most of the first ones have in common that they require a lot of monomer reactions like the networks 1-2-3-5-6-8-9-10 (c) and 1-2-3-4-8-9-10 (d) having five. In contrast the second ones are fast polymer growing networks like 1-2-4-6-10 (a) and 1-2-4-5-10 (b) having just the minimum required first monomer reaction. Therefore the polymer reactions are considered to be more efficient for lower temperatures. This is consistent with the work of Boulangier et al. (2019), in which their monomer network has an effective cluster formation only for the sharp edged temperature of 1000 K. This also explains the trend of most of the monomer required networks to lower values of  $p_{static}$  for temperatures of 900 K to 1000 K. Köhn et al. (2021) stated that for higher temperatures than 1000 K, larger cluster are getting more unstable due to a high evaporation, which might explain the trend of almost all networks to higher deviations for 1100 K.

There is a small difference of roughly one magnitude higher values of  $p_{static}$ , lowering the temperature from 500 K to 400 K. This is considered to be the case due to low collision rates as mentioned in Köhn et al. (2021).

In contrast, the comparison value  $p_{rise}$  as an indicator for the rising section is almost not temperature dependent, except for a few networks that have a jump from 900 K to 1000 K. The reason for this is considered to be the same as for the rising of  $p_{static}$ , the high evaporation rate for high temperatures.

## 4.4 Network combinations

The network optimization was based on the aim of a low deviating combined network for the whole temperature range of  $T = 400, \dots, 1100$  K. The least deviating networks for each temperature are shown in Figure 3.3i for the static section and in Figure 3.4i for the rising section with colored lines. There are five networks in the static section but only four of them were used for the optimization. Since the best network 1-2-3-4-8-10 at  $T = 400$  K is in the same order of magnitude as the networks 1-2-4-6-10 and 1-2-4-5-10 but is almost one order of magnitude worse in the remaining temperature range, it was not considered for the optimization. For the optimization, due to the static section, the networks 1-2-4-6-10 (a) and 1-2-4-5-10 (b) were chosen because they are both similarly covering all temperatures up to  $T = 900$  K. Furthermore, the networks 1-2-3-5-6-8-9-10 (c) and 1-2-3-4-8-9-10 (d) were selected because of their much lower values of  $p_{static}$  at  $T = 1000$  K and  $T = 1100$  K. In the rising section, the comparison value  $p_{rise}$  lead only to two best temperature networks but one of them, (a), has already been considered in the static section. Adding the remaining network 1-2-4-5-6-10 would almost double the number of combination from eleven for four networks to 21 for five networks. Since the value for this network is not significantly lower than the value of network (a), it was also not considered for the optimization.

The main approach of the network optimization was therefore to combine the good low temperature properties of (a) and (b) with the good high temperature properties of (c) and (d).

The results of the combination of networks showed that in the low temperature range, until 800 K, the combination (bc) using 20 reactions was the only combined network, which improved the comparison value  $p_{static}$  but stays within the same orders of magnitude as the networks (a) and (b) using eight reactions. For 1000 K the network (d) is still two orders of magnitude better than any other reduced network. The combination (cd), using 18 reactions, reduced the value of  $p_{static}$  from  $2 \cdot 10^{-3}$  of network (c), using 14 reactions, to  $5 \cdot 10^{-4}$ .

The aim of the optimization was to find a network which is least deviating for the whole temperature range. Therefore, the maximum deviation over the whole temperature range was used to find the optimal network, which is leading to the two networks (ac) using 20 and (acd) using 24 reactions. For both networks, the comparison value  $p_{static}$  stayed below  $2 \cdot 10^{-2}$  for all temperatures and because (ac) has less reactions, it is stated to be the best combined network in the static section.

In the rising section, the most improvements to the value  $p_{rise}$  were made by the combination of all networks (abcd) using 28 reactions. This reduced its value by roughly a factor of three compared to (a) using 8 reactions to  $p_{rise} = 0.5$  for 1000 K and  $p_{rise} = 0.7$  for 1100 K.

The effects of the optimization on the comparison values were compared. It showed that including reactions to a network does not necessarily lead to an improvement in the static section. In contrast, the trend for an improvement within the rising section is high when reactions were included to the network. These statements were also supported by the results Table 3.1, showing the correlation between the comparison value and the number of reactions included in the network. Even the highest correlation for  $p_{static}$  predicts only moderate correlation for 1100 K with  $R = -0.59$ . On the other hand, the correlation for  $p_{rise}$  is moderate with  $R = -0.66$  for less than 1000 K and almost strong with  $R = -0.78$  for 1100 K (Kohn, 2005).

It should be emphasised that there is no correlation predicted for 1000 K in the static section, which offers most opportunities for improvements at this temperature. This is confirmed by the result of network (d), which gives by far the least deviant value for  $p_{static}$  despite the inclusion of only 14 reactions.

# Chapter 5

## Conclusion

This thesis reached its aim of creating a simplified  $\text{TiO}_2$  cluster formation network up to  $(\text{TiO}_2)_{10}$ . 70 reduced networks were constructed by an elimination of clustering reactions. In contrast to the original full polymer network, which is using 50 reactions for building clusters of size 10, the reduced networks are including just 8 to 18. Simulations for these networks were performed, using the closed kinetic nucleation approach of Boulangier et al. (2019), to show that the reduction of reactions affected the cloud particle number density  $n_{CP}$  in the following two ways:

1. Shift in time during the strong rising at the beginning of the simulation. The original network is rising in the order of hours earlier than the reduced networks.
2. Shift in the magnitude of  $n_{CP}$  during the static section, after a few days simulation time, when the rate of  $n_{CP}$  dropped. The original network is between 1 to  $3 \cdot 10^{-6}$  orders of magnitude higher than the reduced networks.

The reduced networks were evaluated regarding to the shift in the magnitude for the temperature range  $T = 400, \dots, 1100$  K. This leads to the four least deviating networks 1-2-4-6-10 (a) with 8 reactions, 1-2-4-5-10 (b) with 8 reactions, 1-2-3-5-6-8-9-10 (c) with 14 reactions and 1-2-3-4-8-9-10 (d) with 12 reactions. The maximum deviation of  $n_{CP}$  over all temperatures was the smallest with  $p_{static} = 10^{-1}$  for network (a) within the static section and with  $p_{rise} = 1.8$  for (b) in the rising section.

In order to keep the maximum deviation of  $n_{CP}$  over all temperatures as low as possible, the above reduced networks were further combined. The combination (ac) with 18 reactions was able to reduce this value to  $p_{static} = 2 \cdot 10^{-2}$  in the static section. In the rising section, the combined network (abcd) with 28 reactions lead to the smallest value of  $p_{rise} = 0.7$ .

The evaluation of the networks (a), (b), (c) (d) and their combinations showed a

temperature dependent correlation between the deviation in  $n_{CP}$  and the number of reactions included in the networks. The analysis stated zero to weak negative correlation for temperatures  $T \leq 1000$  K and moderate negative correlation for  $T = 1100$  K in the static section. For the deviation in the rising section of the simulation, moderate negative correlation was found for  $T \leq 1000$  K and strong negative correlation for  $T = 1100$  K. This offers opportunities of reducing reactions from the cluster formation network in the static section, especially for  $T \leq 1000$  K, without leading to a strong change in the cloud particle number density.

Thus, this work showed a way to simplify the cluster formation process of  $\text{TiO}_2$  and pointed out how it influences the cloud particle number density.

# Bibliography

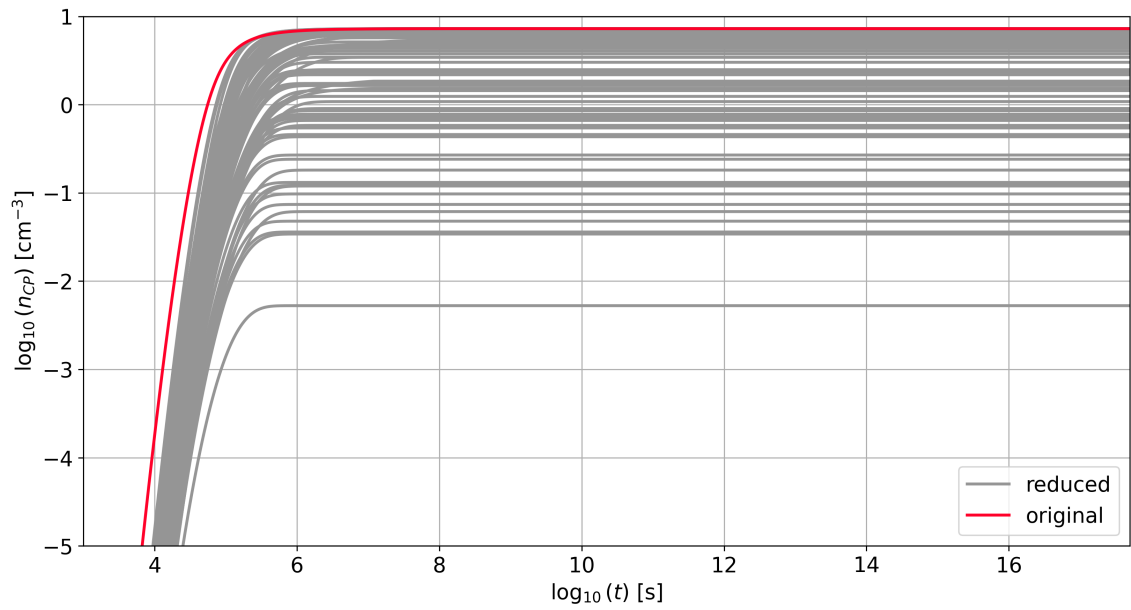
- J. Boulangier, D. Gobrecht, L. Decin, A. de Koter, and J. Yates. Developing a self-consistent AGB wind model - II. Non-classical, non-equilibrium polymer nucleation in a chemical mixture. *Monthly Notices of the Royal Astronomical Society*, 489(4): 4890–4911, 09 2019. ISSN 0035-8711. doi: 10.1093/mnras/stz2358. URL <https://doi.org/10.1093/mnras/stz2358>.
- J. L. Christiansen. Five thousand exoplanets at the nasa exoplanet archive. *Nature Astronomy*, 6:516–519, 2022. doi: 10.1038/s41550-022-01661-8. URL <https://doi.org/10.1038/s41550-022-01661-8>.
- N. Espinoza, B. V. Rackham, A. Jordán, D. Apai, M. López-Morales, D. J. Osip, S. L. Grimm, J. Hoeijmakers, P. A. Wilson, A. Bixel, C. McGruder, F. Rodler, I. Weaver, N. K. Lewis, J. J. Fortney, and J. Fraine. ACCESS: a featureless optical transmission spectrum for WASP-19b from Magellan/IMACS. *Monthly Notices of the Royal Astronomical Society*, 482(2):2065–2087, 10 2018. ISSN 0035-8711. doi: 10.1093/mnras/sty2691. URL <https://doi.org/10.1093/mnras/sty2691>.
- C. Helling. Exoplanet clouds. *Annual Review of Earth and Planetary Sciences*, 47(1):583–606, 2019. doi: 10.1146/annurev-earth-053018-060401. URL <https://doi.org/10.1146/annurev-earth-053018-060401>.
- C. Helling and P. Woitke. Dust in brown dwarfs - v. growth and evaporation of dirty dust grains. *Astronomy & Astrophysics*, 455(1):325–338, 2006. doi: 10.1051/0004-6361:20054598. URL <https://doi.org/10.1051/0004-6361:20054598>.
- A. C. Hindmarsh, J. S. Urban, and J. William. public subroutine dlsode(f, neq, y, t, tout, itol, rtol, atol, itask, istate, iopt, rwork, lrw, iwork, liw, jac, mf). <https://jacobwilliams.github.io/odepack/proc/dlsode.html>, 2023. Accessed: 04.09.2023.
- J. G. Hudson. Cloud condensation nuclei. *Journal of Applied Meteorology and Climatology*, 32(4):596–607, 1993. doi: [https://doi.org/10.1175/1520-0450\(1993](https://doi.org/10.1175/1520-0450(1993)

- 032(0596:CCN)2.0.CO;2. URL [https://journals.ametsoc.org/view/journals/apme/32/4/1520-0450\\_1993\\_032\\_0596\\_ccn\\_2\\_0\\_co\\_2.xml](https://journals.ametsoc.org/view/journals/apme/32/4/1520-0450_1993_032_0596_ccn_2_0_co_2.xml).
- C. Köhn, C. Helling, M. Bødker Enghoff, K. Haynes, J. P. Sindel, D. Krog, and D. Gobrecht. Dust in brown dwarfs and extra-solar planets - viii. tio<sub>2</sub> seed formation: 3d monte carlo versus kinetic approach. *Astronomy & Astrophysics*, 654:A120, 2021. doi: 10.1051/0004-6361/202140378. URL <https://doi.org/10.1051/0004-6361/202140378>.
- W. Kohn. *Statistik: Datenanalyse und Wahrscheinlichkeitsrechnung*. Springer, Berlin and Heidelberg, 2005. ISBN 3-540-21677-4.
- E. Lee, C. Helling, H. Giles, and S. T. Bromley. Dust in brown dwarfs and extra-solar planets - iv. assessing tio<sub>2</sub> and sio nucleation for cloud formation modelling. *Astronomy & Astrophysics*, 575:A11, 2015. doi: 10.1051/0004-6361/201424621. URL <https://doi.org/10.1051/0004-6361/201424621>.
- N. Madhusudhan. Exoplanetary atmospheres: Key insights, challenges, and prospects. *Annual Review of Astronomy and Astrophysics*, 57(1):617–663, 2019. doi: 10.1146/annurev-astro-081817-051846. URL <https://doi.org/10.1146/annurev-astro-081817-051846>.
- M. S. Marley, A. S. Ackerman, J. N. Cuzzi, and D. Kitzmann. Clouds and hazes in exoplanet atmospheres. *arXiv: Earth and Planetary Astrophysics*, 2013. doi: 10.2458/azu\_uapress\_9780816530595-ch15. URL <https://api.semanticscholar.org/CorpusID:117951318>.
- D. Newell and E. Tiesinga. The international system of units (si), 2019 edition, 2019-08-20 2019.
- J. P. Sindel, D. Gobrecht, C. Helling, and L. Decin. Revisiting fundamental properties of tio<sub>2</sub> nanoclusters as condensation seeds in astrophysical environments. *Astronomy & Astrophysics*, 668:A35, dec 2022. doi: 10.1051/0004-6361/202243306. URL <https://doi.org/10.1051/0004-6361/202243306>.
- P. Spyros, N. Nikolov, J. Southworth, S. Constantinou, N. Madhusudhan, A. L. Carter, E. J. W. de Mooij, J. J. Fortney, N. P. Gibson, J. M. Goyal, C. Helling, N. J. Mayne, and T. Mikal-Evans. Transmission spectroscopy with VLT FORS2: a featureless spectrum for the low-density transiting exoplanet WASP-88b. *Monthly Notices of the Royal Astronomical Society*, 506(2):2853–2870, 07 2021. ISSN 0035-8711. doi: 10.1093/mnras/stab1847. URL <https://doi.org/10.1093/mnras/stab1847>.

---

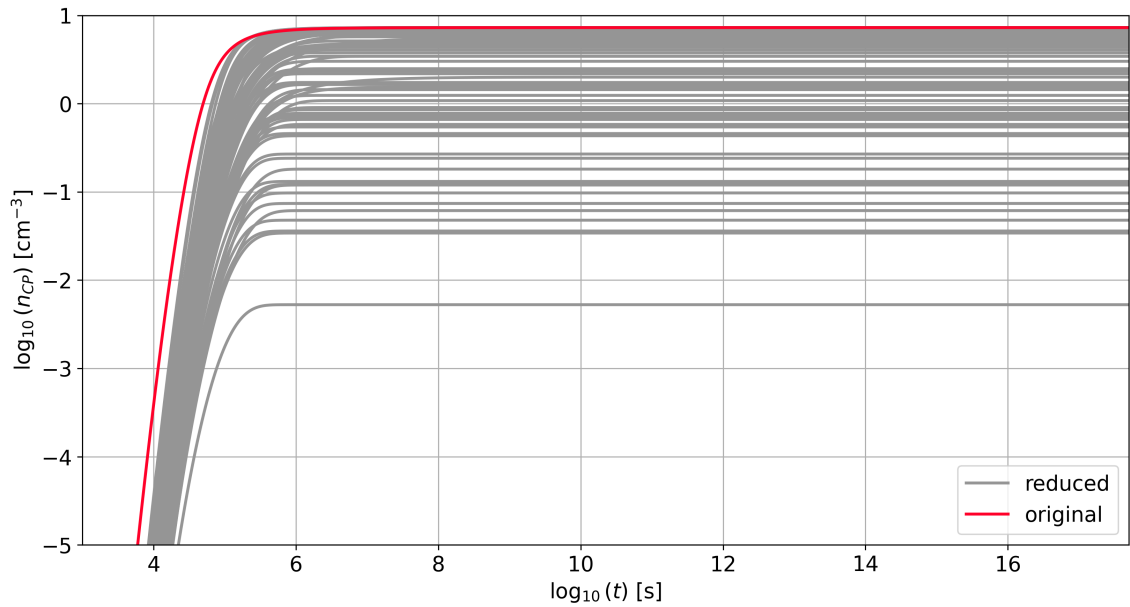
S. Tsai, J. R. Lyons, L. Grosheintz, P. B. Rimmer, D. Kitzmann, and K. Heng. Vulcan: An open-source, validated chemical kinetics python code for exoplanetary atmospheres. *The Astrophysical Journal Supplement Series*, 228(2):20, feb 2017. doi: 10.3847/1538-4365/228/2/20. URL <https://dx.doi.org/10.3847/1538-4365/228/2/20>.

# Appendix

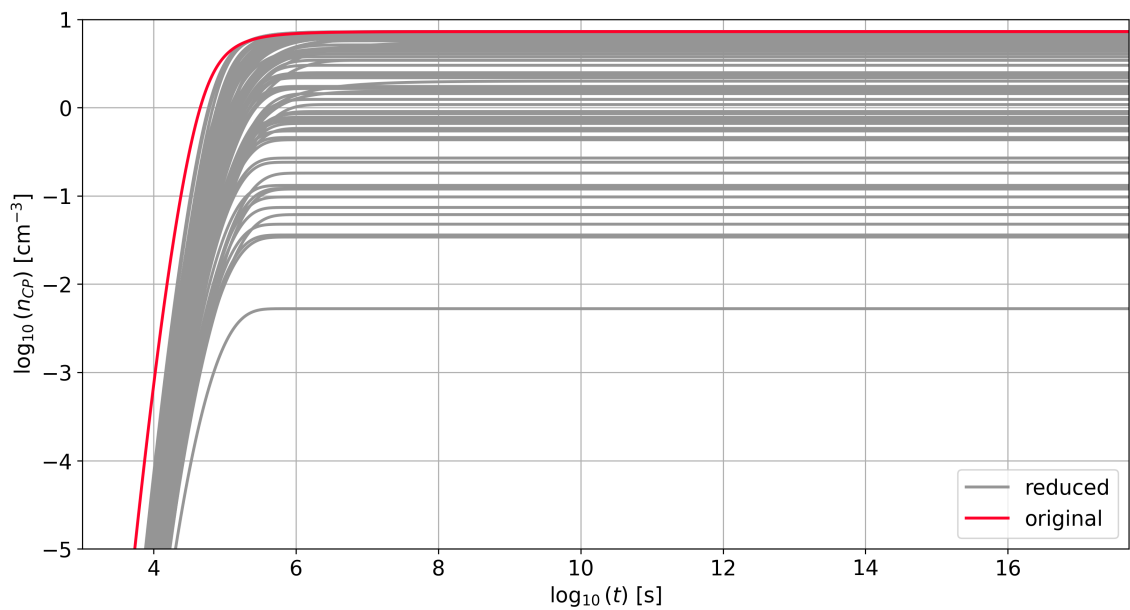


(i) 400 K

Figure 5.1: Logarithmic cloud particle number densities over logarithmic time is shown for each temperature  $T = 400, 500, \dots, 1100$  K. The original network (red line) is shown with all 70 path networks (grey lines) for values above  $10^{-5} \text{ cm}^{-3}$  and up to  $5 \cdot 10^{17} \text{ s}$ .

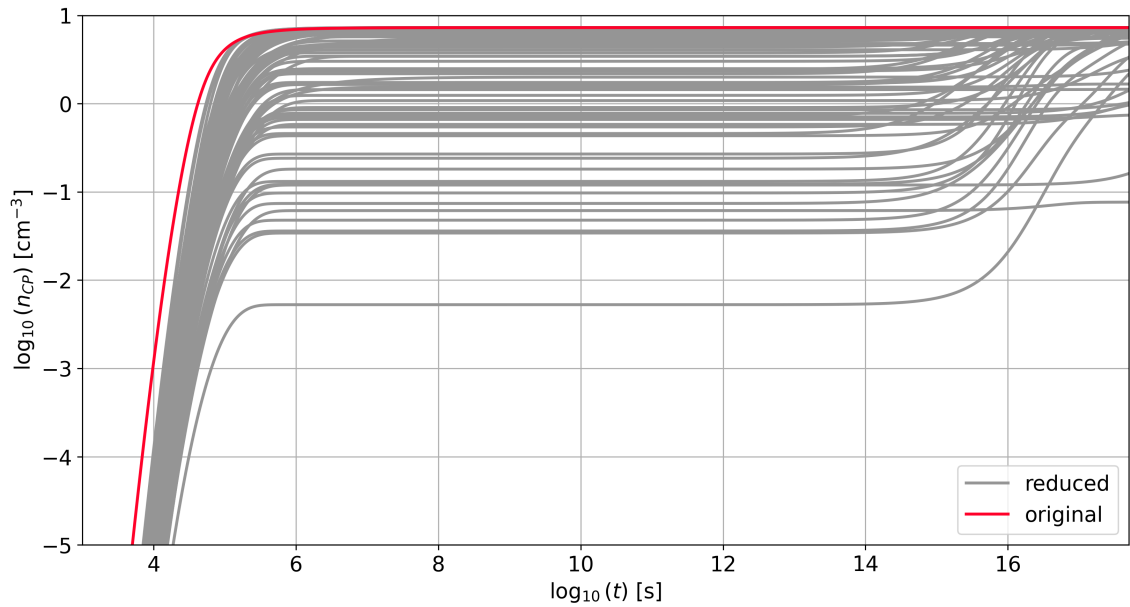


(ii) 500 K

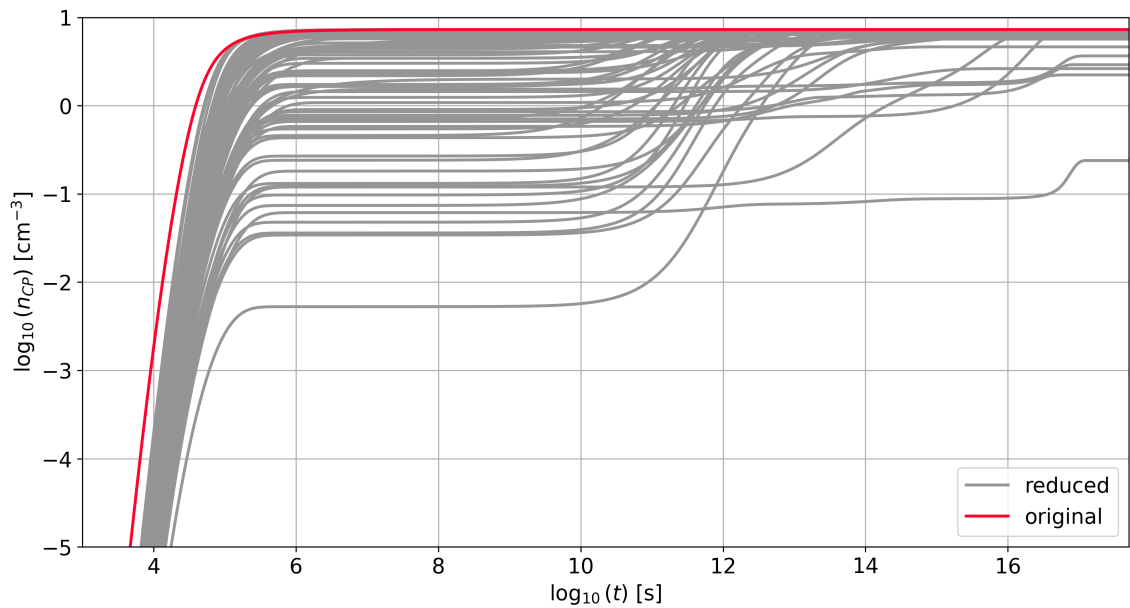


(iii) 600 K

Figure 5.1: Logarithmic cloud particle number densities over logarithmic time is shown for each temperature  $T = 400, 500, \dots, 1100$  K. The original network (red line) is shown with all 70 path networks (grey lines) for values above  $10^{-5} \text{ cm}^{-3}$  and up to  $5 \cdot 10^{17}$  s. (continued)

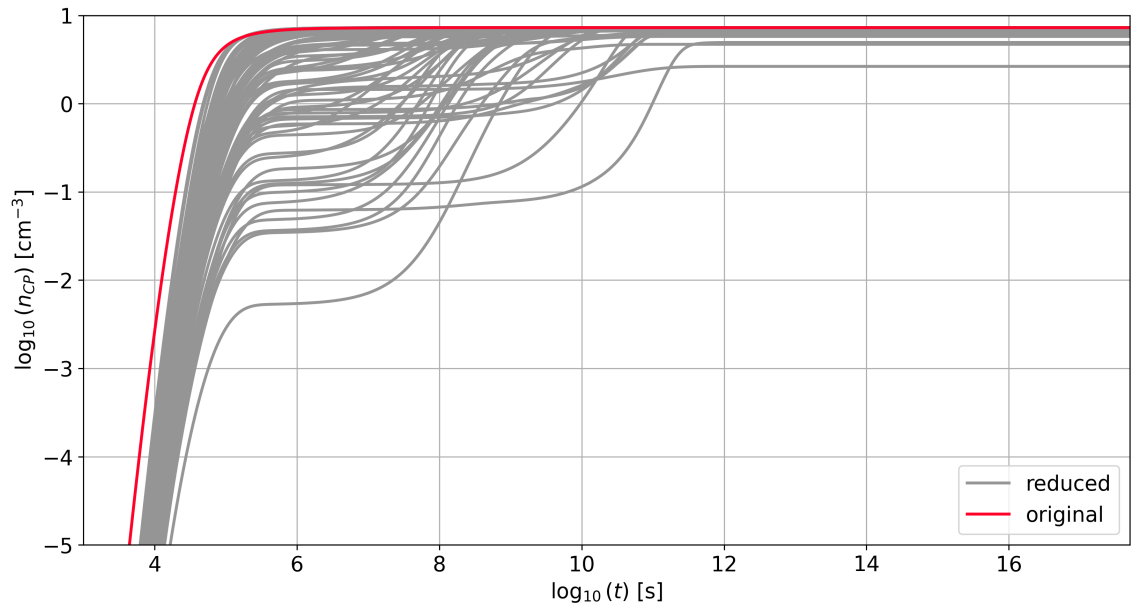


(iv) 700 K

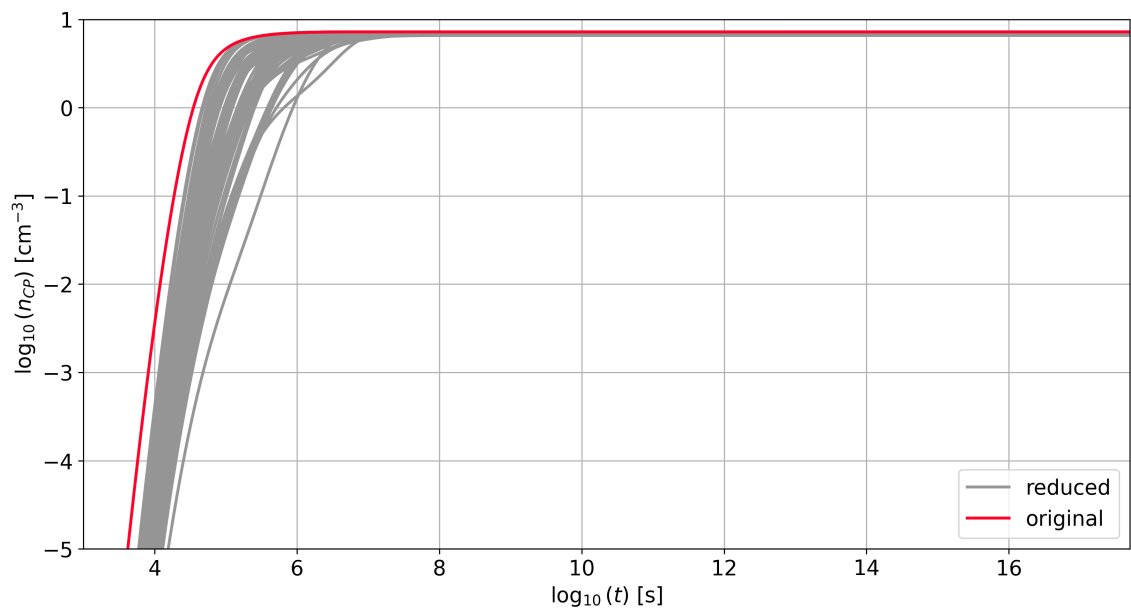


(v) 800 K

Figure 5.1: Logarithmic cloud particle number densities over logarithmic time is shown for each temperature  $T = 400, 500, \dots, 1100$  K. The original network (red line) is shown with all 70 path networks (grey lines) for values above  $10^{-5} \text{ cm}^{-3}$  and up to  $5 \cdot 10^{17}$  s. (continued)

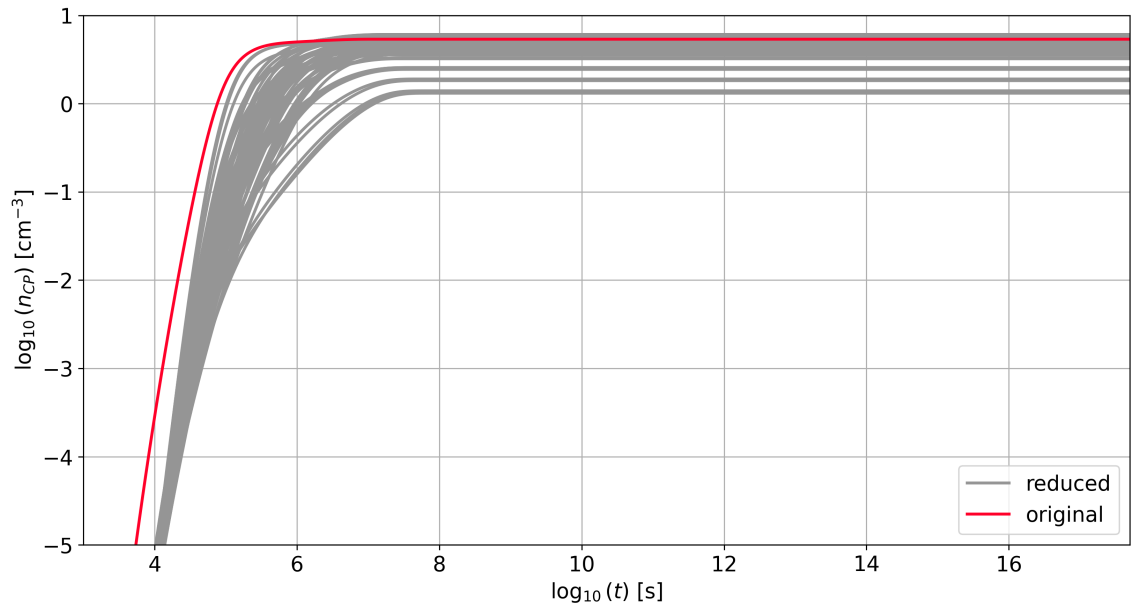


(vi) 900 K



(vii) 1000 K

Figure 5.1: Logarithmic cloud particle number densities over logarithmic time is shown for each temperature  $T = 400, 500, \dots, 1100$  K. The original network (red line) is shown with all 70 path networks (grey lines) for values above  $10^{-5} \text{ cm}^{-3}$  and up to  $5 \cdot 10^{17}$  s. (continued)



(viii) 1100 K

Figure 5.1: Logarithmic cloud particle number densities over logarithmic time is shown for each temperature  $T = 400, 500, \dots, 1100$  K. The original network (red line) is shown with all 70 path networks (grey lines) for values above  $10^{-5} \text{ cm}^{-3}$  and up to  $5 \cdot 10^{17}$  s. (continued)

# Declaration

I declare that I have authored this thesis independently, that I have not used other than the declared sources/resources, and that I have explicitly indicated all material which has been quoted either literally or by content from the sources used. The text document uploaded to UNIGRAZonline or TUGRAZonline is identical to the present bachelor's thesis.

*Graz, September 28, 2023*

---